EDGE ARTICLE

Check for updates

All publication charges for this article have been paid for by the Royal Society of Chemistry

Vanadium-regulated nickel phosphide nanosheets for electrocatalytic sulfion upgrading and hydrogen production†

Rui-Qing Li, [iD] * Xiaojun Wang, Shuixiang Xie, Songyun Guo, Zhe Cao, Zhenhao Yan, Wei Zhang* and Xiaoyu Wan*

The electrochemical sulfion oxidation reaction (SOR) is highly desirable to treat sulfion-rich wastewater and achieve energy-saving hydrogen production when coupled with the cathodic hydrogen evolution reaction (HER). Herein, we propose a thermodynamically favorable SOR to couple with the HER, and develop vanadium-doped nickel phosphide (V-Ni$_2$P) nanosheets for simultaneously achieving energy-efficient hydrogen production and sulfur recovery. V doping can efficiently adjust the electronic structure and improve intrinsic activity of Ni$_2$P, which exhibits outstanding electrocatalytic performances for the HER and SOR with low potentials of −0.093 and 0.313 V to afford 10 mA cm^{-2}. Remarkably, the assembled V-Ni$_2$P-based hybrid water electrolyzer coupling the HER with the SOR requires small cell voltages of 0.389 and 0.834 V at 10 and 300 mA cm^{-2}, lower than those required in a traditional water electrolysis system (1.5 and 1.969 V), realizing low-cost sulfion upgrading to value-added sulfur and hydrogen generation. This work provides an approach for energy-saving hydrogen production and toxic waste degradation.

Introduction

Hazardous sulfion-containing wastewater is produced in various industries, such as dyeing, papermaking and printing industries, and poses severe hazards to the ecological environment and human health.[1,2] At present, traditional strategies such as chemical deposition, oxidation, and biochemical methods have been used to treat such wastewater.[3,4] However, high chemical consumption, product recovery deficiency and high expenses have puzzled researchers. The electrochemical sulfion oxidation reaction (SOR, S^{2-} → S + 2e$^-$) at the anode powered by intermittent and unstable renewable electricity is an attractive technology to treat sulfur-rich wastewater and generate valuable sulfur species under mild conditions due to its mild operation conditions and simplicity.[5,6] Meanwhile, the SOR possesses a low thermodynamic oxidation potential (0.142 V *vs.* the reversible hydrogen electrode, RHE, pH = 14) due to the presence of electron-donating S^{2-}, which can significantly decrease the energy expense.[7] In general, the SOR process involves complex polysulfide intermediate formation with a sixteen-electron transfer process, leading to sluggish catalytic kinetics.[8,9] Recently, although considerable efforts have been devoted to exploiting high-performance SOR catalysts

such as metal oxides and metal chalcogenides, the efficiency needs further enhancement. The primary reason is that sulfur species tend to poison and corrode metallic catalysts, decreasing catalytic activity and stability.[10] To this end, some researchers have developed different strategies including heteroatom doping, heterostructure construction and carbon coating to adjust the electronic structure, modify adsorption energy of reaction intermediates, and improve structural stability, thereby boosting catalytic performances of catalysts.[11–14] Nevertheless, relevant studies toward the SOR are still limited and it is urgent to explore efficient catalysts to realize sulfion degradation and upcycling of sulfur products.

In general, the hydrogen evolution reaction (HER) occurs at the cathode during the electrocatalytic treatment of sulfur-rich wastewater, which generates ideal hydrogen (H$_2$) energy which is carbon free and environmentally friendly, and has high-energy density.[15,16] As we know, the alkaline HER suffers from sluggish reaction kinetics and requires large overpotentials compared with that in acidic electrolyte, which limits its practical applications.[17] To lower the overpotentials, many efforts have been devoted to exploiting efficient electrocatalysts.[18–20] Precious Pt-based materials are considered to be advanced HER catalysts, and the limited reserves and high price are not beneficial for their industrialization.[21,22] Moreover, most developed catalysts have monofunctional catalytic performance, which may cause incompatibility and deterioration of catalysts and the doubling cost of synthesis when paired with a mono-functional catalyst.[23,24] Constructing

School of Textile and Clothing, Nantong University, Nantong 226019, PR China. E-mail: liruiqing@ntu.edu.cn; zhangwei@ntu.edu.cn; 2022081@ntu.edu.cn

a bifunctional catalyst is promising to achieve low-energy H_2 production and sulfion upgrading by combining the HER with the SOR.[25,26]

Herein, we devise a phosphide electrocatalyst of V-doped Ni_2P nanosheets on a nickel foam (NF) substrate (V-Ni_2P) toward efficient HER and SOR processes. Due to the optimized electronic structure induced by V doping and uniform nanosheet structure, V-Ni_2P displays excellent catalytic activities for the HER and SOR with low potentials of 0.093 and 0.313 V at 10 mA cm^{-2}. The assembled V-Ni_2P-based hybrid water electrolysis (HWE) system coupling the HER with the SOR requires quite low cell voltages, which achieve simultaneous low-energy H_2 production and sulfur ion upcycling to valuable sulfur products.

Results and discussion

Synthesis and structural characterization

The V-Ni_2P nanosheets on a NF substrate are prepared *via* a hydrothermal–phosphorization reaction, as displayed in Fig. 1a. The NF substrate possesses high conductivity, good connectivity and large surface area, and can accelerate adhesion and mass transfer of active components. Initially, a Ni-based layered double hydroxide (NiV LDH) nanosheet precursor on NF is obtained by a hydrothermal process. The phase structure of NiV LDH analyzed by X-ray diffraction (XRD) exhibits several characteristic diffraction peaks of LDH except for strong diffraction peaks of NF (Fig. S1†). The scanning electron microscopy (SEM) images (Fig. 1b and c) show that uniform NiV LDH nanosheets are vertically grown on the NF surface. Then, NaH_2PO_2 is applied as the phosphorus source to convert the NiV LDH nanosheet precursor into the V-Ni_2P product. As shown in Fig. 1d, the clear diffraction peaks of V-Ni_2P can be assigned to Ni_2P (PDF#74-1385) in the absence of any additional peaks, confirming the formation of V-Ni_2P. Moreover, V-Ni_2P still maintains nanosheet-like morphology (Fig. 1e) and the transmission electron microscope (TEM) image further confirms the two-dimensional nanosheet structure (Fig. 1f). The high-resolution TEM (HRTEM) image reveals obvious lattice fringes with a 0.223 nm interplanar distance, which indexes to the (111) plane of V-Ni_2P (Fig. 1g). The SEM and corresponding element mapping images (Fig. 1h–k) reflect that V-Ni_2P is composed of Ni, V, and P elements, homogeneously distributed on the surface of whole nanosheets.

The surface composition and chemical states of V-Ni_2P are analyzed by X-ray photoelectron spectroscopy (XPS). As displayed in Fig. 2a, the survey XPS spectrum of V-Ni_2P suggests the presence of Ni, V and P elements. As shown in Fig. 2b, the Ni 2p spectrum of V-Ni_2P exhibits two characteristic peaks at 852.2, 856.3 eV and 869.1, 874.1 eV, which are attributed to Ni $2p_{3/2}$ and Ni $2p_{1/2}$, respectively.[27] Notably, the binding energy of the Ni 2p spectrum shows a negative shift of 0.2 eV in comparison with that of Ni_2P, reflecting the increased electron density of Ni after V doping and the presence of electronic interaction and redistribution between Ni and V because of higher electronegativity of Ni compared with of V.[28] In a typical V 2p spectrum (in

Fig. 2c), two peaks at 516.6 eV and 524.0 eV are assigned to V $2p_{3/2}$ and V $2p_{1/2}$ of V–P bonds, manifesting successful V doping.[28] The P 2p spectrum of V-Ni_2P (Fig. 2d) has typical peaks at 128.8 and 129.7 eV, belonging to P $2p_{3/2}$ and P $2p_{1/2}$ of P-based species. The peak at 133.9 eV is assigned to the P–O bond of oxidized phosphide species due to the exposure to air.[29] The above results manifest that V-doping can regulate the electronic structure of Ni_2P and optimize the catalytic reaction energy barrier.

Electrochemical performances

The electrocatalytic performances of V-Ni_2P for the HER are evaluated in 1.0 M NaOH by using a three-electrode system. In the HER polarization curves (Fig. 3a, f and S2†), V-Ni_2P has superior catalytic performances, greatly higher than those of Ni_2P, V-Ni_2P-1 and V-Ni_2P-2. V-Ni_2P delivers the smallest overpotentials (η_{10} and η_{400}) of 93 and 294 mV to attain current densities of 10 and 400 mA cm^{-2} compared with Ni_2P, V-Ni_2P-1, V-Ni_2P-2 and many reported catalysts (Fig. 3g and Table S1†), manifesting its outstanding HER performance. The Tafel slope derived from HER curves can reflect its kinetics and as depicted in Fig. 3b and f, V-Ni_2P possesses a small value of Tafel slope (81 mV dec^{-1}). The low value for V-Ni_2P indicates rapidly increased current densities with increasing overpotentials.[30,31] The electrochemical active area (ECSA) is evaluated to elucidate the actual area of the catalyst by using the electrochemical double-layer capacitance (C_{dl}), which is calculated by cycle voltammetry (CV) measurements at various scan rates (Fig. S3†). The C_{dl} of V-Ni_2P is computed to be 10.8 mF cm^{-2}, larger than that of Ni_2P (6.8 mF cm^{-2}, Fig. 3c and f), indicating that the number of catalytic sites and ECSA increase after V doping.[32] Moreover, the polarization curve normalized by using ECSA is widely accepted to analyze the inherent activity. As shown in Fig. 3d, the ECSA-normalized curves exhibit higher intrinsic activity for V-Ni_2P compared with Ni_2P. The boosted performance can be ascribed to the optimization of energy barriers for adsorption and dissociation of H_2O and free energy of adsorbed hydrogen (H*) after V introduction.[33] The charge transfer kinetics is further analyzed by electrochemical impedance spectroscopy (EIS). In the Nyquist diagram (Fig. 3e), V-Ni_2P has a lower charge transfer impedance (R_{CT}, 1.4 Ω) compared with Ni_2P (2.0 Ω), revealing the fast charge transfer rate of V-Ni_2P. V-Ni_2P has high faradaic efficiency by comparing the generated gas amount with the theoretical gas amount (Fig. S4†), indicating that the catalytic currents are derived entirely from the intended catalytic reaction. Besides, the chronopotentiometry (v–t) test is conducted to assess HER stability. As displayed in Fig. 3h, V-Ni_2P reveals excellent HER durability with almost constant potential after the 50 h test. Meanwhile, the post-HER measurements (Fig. S5–S7†) show that the phase and morphology of V-Ni_2P nanosheets are well maintained, and the Ni, V, and P elements are uniformly distributed on the surface of nanosheets. As shown in Fig. S8,† the binding energies of Ni 2p and V 2p have no significant variation, and the peak intensity of the P 2p spectrum decreases slightly
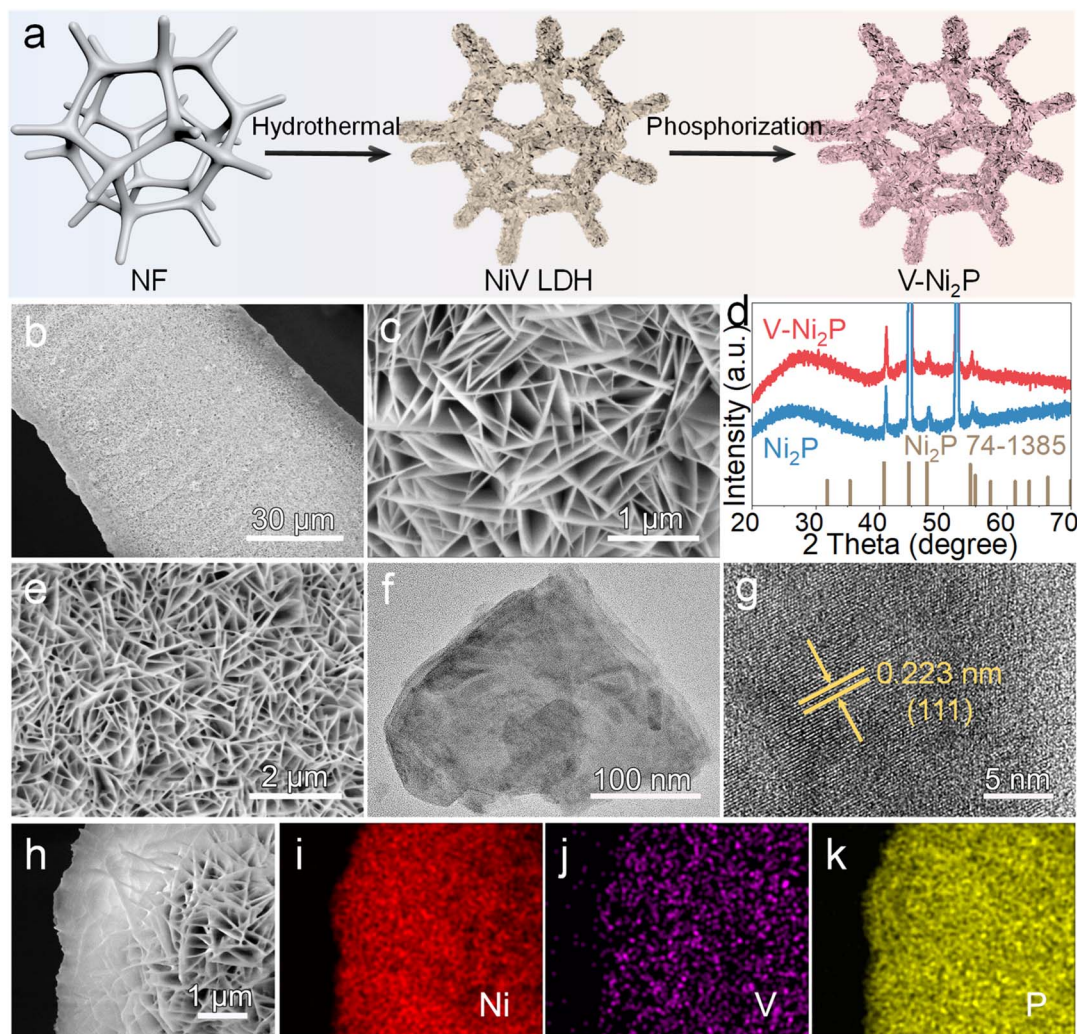
Fig. 1 (a) Schematic illustration for fabrication of V-Ni$_2$P. (b and c) SEM images of the NiV LDH precursor. (d) XRD patterns of Ni$_2$P and V-Ni$_2$P. (e) SEM, (f) TEM, (g) HRTEM, (h–k) SEM and corresponding element mapping images of V-Ni$_2$P.
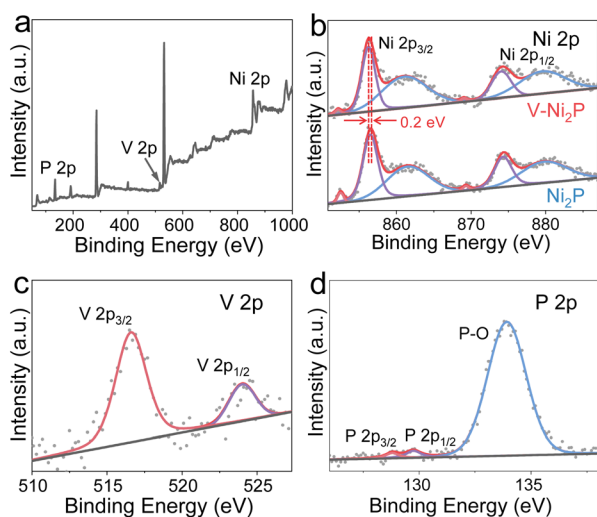

Fig. 2 (a) Survey XPS, (b) Ni 2p, (c) V 2p and (d) P 2p spectra of V-Ni$_2$P.

probably due to its partial dissolution in the electrolyte during a long-term test.[34]

We further study the SOR properties of prepared samples in 1.0 M NaOH with a concentration of 1.0 M Na$_2$S. As displayed in Fig. 4a and d, V-Ni$_2$P exhibits outstanding SOR activity with ultralow potentials (η_{10} and η_{200}) of 0.313 and 0.52 V to achieve current densities of 10 and 200 mA cm^{-2}, smaller than those of Ni$_2$P (0.394 and 0.62 V) and many previously reported catalysts (Fig. S9 and Table S2†). As shown in Fig. 4b, the Tafel slopes indicate that V-Ni$_2$P shows a smaller slope value (132 mV dec^{-1}) than Ni$_2$P (157 mV dec^{-1}), meaning the improved SOR kinetics of V-Ni$_2$P after V doping. Moreover, the V-Ni$_2$P exhibits good oxygen evolution reaction (OER) activity with smaller potentials of 1.505 and 1.646 V to reach 10 and 200 mA cm^{-2} (Fig. 4c and d) compared with those of Ni$_2$P (1.536, 1.672 V) in the absence of sulfion (1 M NaOH solution). The above result confirms that the V doping can effectively promote SOR and OER performances. Despite achieving splendid OER performances for V-Ni$_2$P, the OER process still needs high potentials
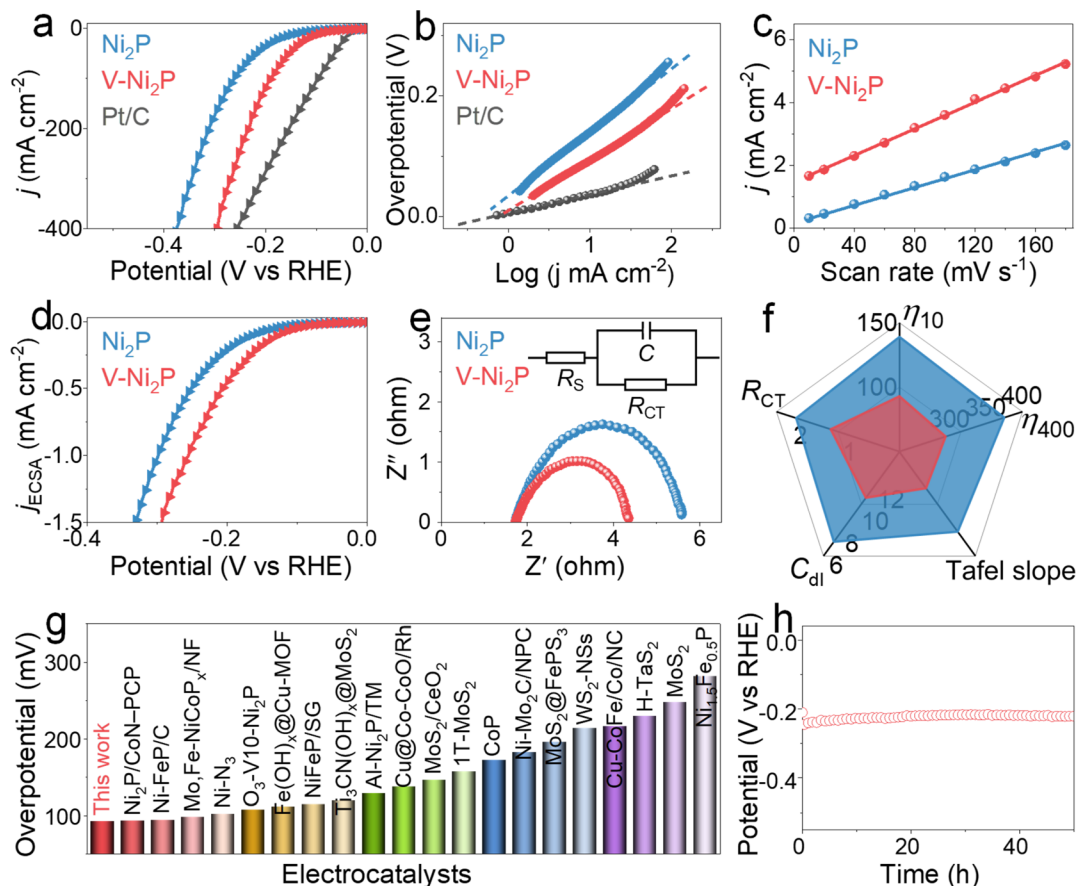
Fig. 3 (a) Polarization curves and (b) corresponding Tafel plots of different catalysts for the HER. (c) C_{dl} values, (d) ECSA-normalized polarization curves, (e) EIS plots and (f) HER performance radar chart of Ni_2P and $V-Ni_2P$. (g) Overpotential comparison of $V-Ni_2P$ with reported catalysts. (h) Durability test of $V-Ni_2P$.

compared with the SOR, which inevitably increases electricity consumption. Coupling the SOR with the HER not only reduces the voltages of hydrogen production, but also enables toxic sulfion degradation.[35] The v–t curve reveals high potential retention within 50 h tests, indicating its remarkable stabilities for the SOR (Fig. 4e) and OER (Fig. S10†). After the OER and SOR stability measurements, the phase, morphology and chemical states are further studied. For the OER, although the morphology is well maintained (Fig. S11†) the peak intensity of the XRD pattern reduces due to partial dissolution of phosphide (Fig. S12†). The Ni XPS spectrum reveals the disappearance of Ni–P (851.8 eV) and the increased content of oxidized species (Fig. 4f), indicating its good OER performance, which is connected to the synergistic effect of phosphide and outer-layer oxides formed in the OER. Moreover, the peak of the V 2p spectrum almost disappears because of its dissolution and reconstruction at large oxidation potentials. For the SOR, the phase (Fig. S13†), morphology (Fig. S14†), composition (Fig. S15†) and chemical states (Fig. 4f–h) of V-Ni_2P are almost preserved, further confirming its long-lasting stability for the SOR.

Based on the remarkable catalytic activities of V-Ni_2P, the two-electrode water electrolyzer with V-Ni_2P as both the anode and cathode is constructed in 1 M NaOH with and without 1 M Na_2S, as displayed in Fig. 5a. As shown in Fig. 5b, the polarization curve of HWE can output higher current densities than conventional overall water splitting (OWS) at the same cell voltages, demonstrating the important role of the SOR in obtaining small cell voltages. Specifically, the HWE system delivers low voltages (V_{10}, V_{100}, and V_{300}) of 0.389, 0.644 and 0.834 V at 10, 100 and 300 mA cm^{-2} (Fig. 5c), much smaller than those needed in the OWS system (1.5, 1.786, and 1.969 V) and most SOR-assisted HWE systems (Fig. 5d and Table S3†). The durability tests of the HWE and OWS are carried out using the v–t measurements at 200 mA cm^{-2}. Remarkably, the applied cell voltages show negligible variation during continuous electrolysis for 100 h (Fig. 5e), implying the preeminent stability of V-Ni_2P. After the HWE stability test, the solid yellow sulfur powders are harvested by acidifying the electrolyte, which is confirmed by the XRD pattern (Fig. 5e and f). Meanwhile, the nanosheet-like morphologies of V-Ni_2P are well maintained (Fig. S16†), indicating its remarkable structure robustness. These results indicate that the SOR-assisted HWE system not only realizes H_2 production at low cell voltages, but also degrades sulfion to elemental sulfur.
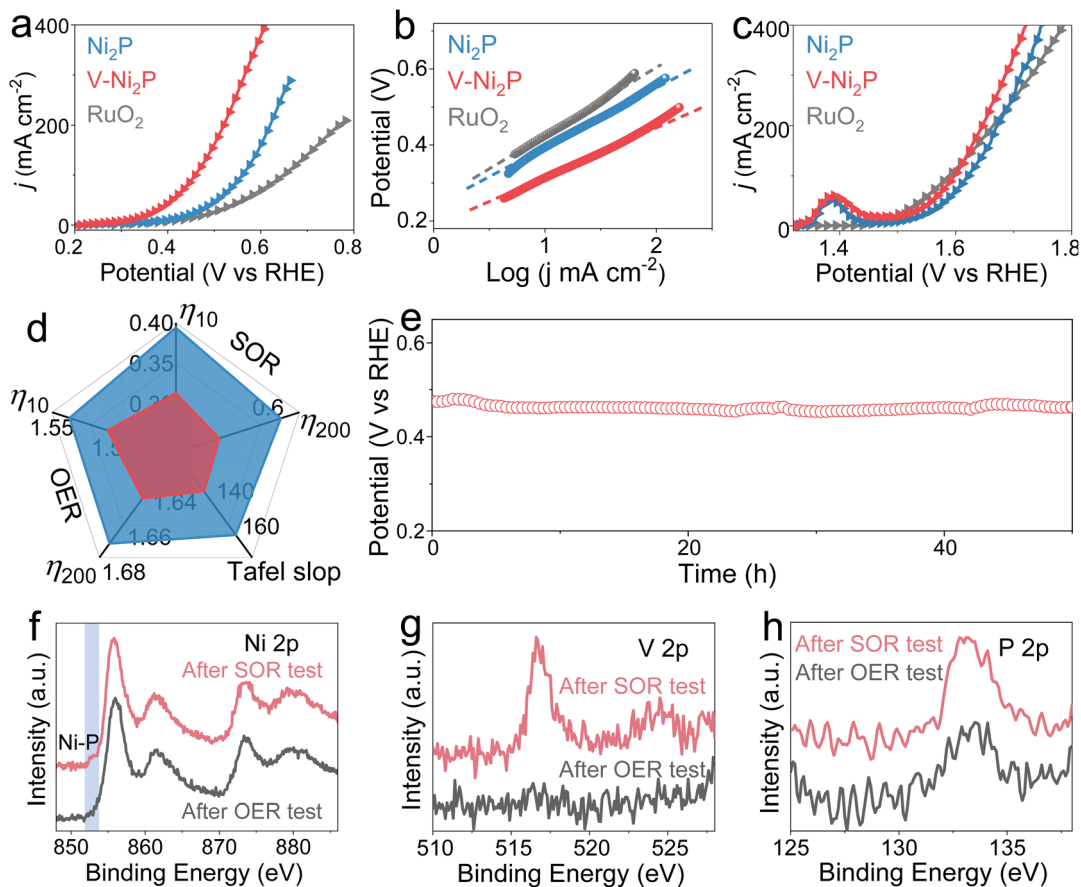
Fig. 4 Polarization curves of the (a) SOR, (b) corresponding Tafel plots and (c) OER of the catalysts. (d) SOR and OER performance radar chart of Ni$_2$P and V–Ni$_2$P. (e) Durability test of V–Ni$_2$P. XPS spectra of (f) Ni 2p, (g) V 2p and (h) P 2p after SOR and OER tests.
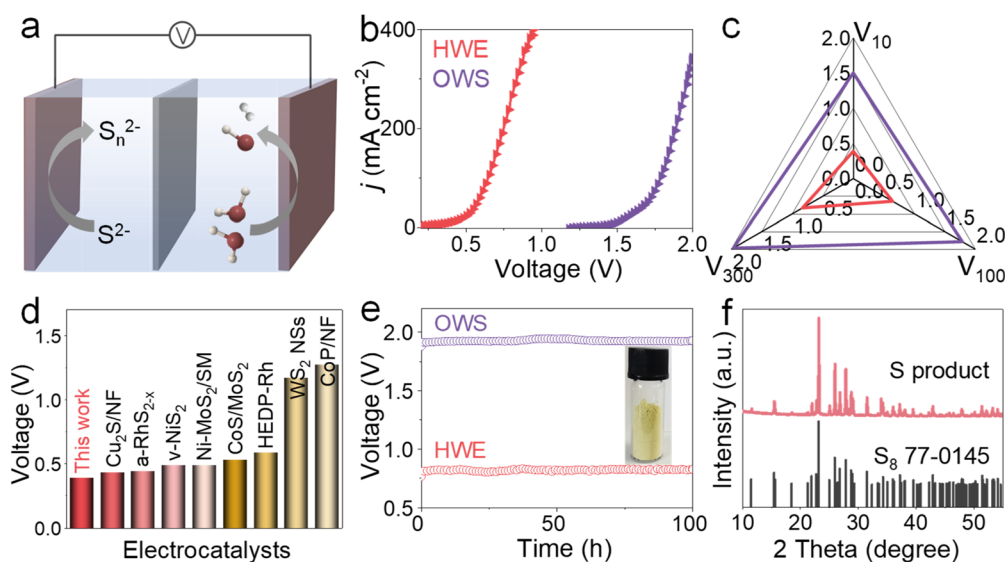

Fig. 5 (a) Schematic illustration of the assembled two-electrode HWE electrolyzer. (b) Polarization curves and durability tests of HWE and OWS systems. Voltage comparison of V–Ni$_2$P with (c) HWE and OWS systems at 10, 200 and 300 mA cm^{-2}, and (d) recently exploited catalysts. (e) Durability test of V–Ni$_2$P for OWS and HWE. Inset: digital image of the S product. (f) XRD pattern of the collected S product.

Conclusions

In summary, V-Ni$_2$P is synthesized by a simple hydrothermal and phosphorization process, and possesses outstanding electrocatalytic performances towards the HER and SOR due to the synergistic effect of the uniform nanosheet structure and optimized reaction energy barrier by V introduction. Therefore, V-Ni$_2$P requires small potentials of 0.093 and 0.313 V at 10 mA cm^{-2} for the HER and SOR. Remarkably, the assembled V-Ni$_2$P-based HWE system needs low cell voltages of 0.389 and 0.834 V to reach 10 and 300 mA cm^{-2}, significantly smaller than those needed in the OWS system (1.5 and 1.969 V), realizing low-energy H$_2$ production and sulfion upcycling to sulfur products. This work provides a facile route to construct bifunctional electrodes for highly efficient H$_2$ generation and sulfion utilization of sulfur-containing wastewater.

Data availability

The relevant experimental and characterization data are available in the article and the ESI.†

Author contributions

Rui-Qing Li: conceptualization, writing – review & editing. Xiaojun Wang: investigation. Shuixiang Xie: data curation, formal analysis. Songyun Guo: formal analysis. Zhenhao Yan: investigation. Wei Zhang: formal analysis. Xiaoyu Wan: conceptualization, writing – review & editing.

Conflicts of interest

There are no conflicts to declare.

Acknowledgements

Notes and references

1 L. Zhang, Z. Wang and J. Qiu, *Adv. Mater.*, 2022, **34**, e2109321.
2 S. Zhang, Q. Zhou, Z. Shen, X. Jin, Y. Zhang, M. Shi, J. Zhou, J. Liu, Z. Lu and Y. Zhou, *Adv. Funct. Mater.*, 2021, **31**, 2101922.
3 E. Vaiopoulou, T. Provijn, A. Prevoteau, I. Pikaar and K. Rabaey, *Water Res.*, 2016, **92**, 38–43.
4 Y. Pei, J. Cheng, H. Zhong, Z. Pi, Y. Zhao and F. Jin, *Green Chem.*, 2021, **23**, 6975.
5 L. Yi, Y. Ji, P. Shao, J. Chen, J. Li, H. Li, K. Chen, X. Peng and Z. Wen, *Angew. Chem., Int. Ed.*, 2021, **60**, 21550.
6 L. Zhang, Z. Wang and J. Qiu, *Adv. Mater.*, 2022, **34**, 2109321.
7 Y. Pei, D. Li, C. Qiu, L. Yan, Z. Li, Z. Yu, W. Fang, Y. Lu and B. Zhang, *Angew. Chem., Int. Ed.*, 2024, **136**, e202411977.
8 W. Wang, Q. Mao, S. Jiang, K. Deng, H. Yu, Z. Wang, Y. Xu, L. Wang and H. Wang, *Appl. Catal., B*, 2024, **340**, 123194.
9 J. Huo, Q. Liu, X. Liu, X. Cheng, D. Chen, N. Li, K. Liao, Q. Xu and J. Lu, *ACS Mater. Lett.*, 2024, **6**, 2633.
10 T. Wang, X. Cao and L. Jiao, *Angew. Chem., Int. Ed.*, 2022, **61**, e202213328.
11 M. Ahsan, T. He, J. Noveron, K. Reuter, A. Puente-Santiago and R. Luque, *Chem. Soc. Rev.*, 2022, **51**, 812.
12 R. Li, S. Zeng, B. Sang, C. Xue, K. Qu, Y. Zhang, W. Zhang, G. Zhang, X. Liu, J. Deng, O. Fontaine and Y. Zhu, *Nano Res.*, 2023, **16**, 2543.
13 Z. Yang, C. Zhao, Y. Qu, H. Zhou, F. Zhou, J. Wang, Y. Wu and Y. Li, *Adv. Mater.*, 2019, **31**, 1808043.
14 B. You and Y. Sun, *Acc. Chem. Res.*, 2018, **51**, 1571.
15 R. Li, S. Guo, X. Wang, X. Wan, S. Xie, Y. Liu, C. Wang, G. Zhang, J. Cao, J. Dai, M. Ge and W. Zhang, *Chem. Sci.*, 2024, **15**, 10084.
16 R. Li, H. Su, S. Xie, X. Wan, C. Wang, G. Zhang, M. Ge, J. Dai, C. Xue, C. Li, J. Cao and W. Zhang, *Rare Met.*, 2024, **43**, 6426.
17 X. Deng, X. Zheng, Z. Gong, W. Tan and X. Pei, *Chin. J. Rare Met.*, 2023, **47**, 43.
18 Y. Wang, D. Wang and Y. Li, *Adv. Mater.*, 2021, **33**, 2008151.
19 R. Li, B. Wang, T. Gao, R. Zhang, C. Xu, X. Jiang, J. Zeng, Y. Bando, P. Hu, Y. Li and X. Wang, *Nano Energy*, 2019, **58**, 870.
20 Q. Yao, Z. Yu, L. Li and X. Huang, *Chem. Rev.*, 2023, **123**, 9676.
21 L. Li, G. Zhang, C. Zhou, F. Lv, Y. Tan, Y. Han, H. Luo, D. Wang, Y. Liu, C. Shang, L. Zeng, Q. Huang, R. Zeng, N. Ye, M. Luo and S. Guo, *Nat. Commun.*, 2024, **15**, 4974.
22 K. Stoerzinger, L. Qiao, M. Biegalski and Y. Shao-Horn, *J. Phys. Chem. Lett.*, 2014, **5**, 1636.
23 R. Li, C. Wang, S. Xie, T. Hang, X. Wan, J. Zeng and W. Zhang, *Chem. Commun.*, 2023, **59**, 11512.
24 Z. Wang, N. Zhou, J. Wang, D. Wang, J. Zeng, H. Zhong and X. Zhang, *ChemSusChem*, 2024, **17**, e202301050.
25 Z. Yu, D. Boukhvalov, H. Tan, D. Xiong, C. Feng, J. Wang, W. Wang, Y. Zhao, K. Xu, W. Su, X. Xiang, F. Lin, H. Huang, F. Zhang, L. Zhang, L. Meng and L. Liu, *Chem. Eng. J.*, 2024, **494**, 153094.
26 Z. Xiao, C. Lu, J. Wang, Y. Qian, B. Wang, Q. Zhang, A. Tang and H. Yang, *Adv. Funct. Mater.*, 2023, **33**, 2212183.
27 X. Wang, Q. Hu, G. Li, S. Wei, H. Yang and C. He, *J. Mater. Chem. A*, 2021, **9**, 15648.
28 L. Wen, J. Yu, C. Xing, D. Liu, X. Lyu, W. Cai and X. Li, *Nanoscale*, 2019, **11**, 4198.
29 S. Chen, C. Wang, S. Liu, M. Huang, J. Lu, P. Xu, H. Tong, L. Hu and Q. Chen, *J. Phys. Chem. Lett.*, 2021, **12**, 4849.
30 M. Deng, M. Li, S. Jiang, Y. Nie, L. Li and Z. Wei, *J. Phys. Chem. Lett.*, 2022, **13**, 1069.

31 B. Sang, Y. Liu, X. Wan, S. Xie, G. Zhang, M. Ge, J. Dai, W. Zhang and R. Li, *Chem. Commun.*, 2023, **59**, 8743.

32 C. Zhang, X. Wang, R. Zhao, F. Ndayisenga and Z. Yu, *Chem. Sci.*, 2024, **15**, 1894.

33 L. Li, S. Liu, C. Zhan, Y. Wen, Z. Sun, J. Han, T. Chan, Q. Zhang, Z. Hu and X. Huang, *Energy Environ. Sci.*, 2023, **16**, 157.

34 S. Lu, C. Cheng, Y. Shi, Y. Wu, Z. Zhang and B. Zhang, *Proc. Natl. Acad. Sci. U. S. A.*, 2023, **120**, e2300549120.

35 C. Lyu, Y. Li, J. Cheng, Y. Yang, K. Wu, J. Wu, H. Wang, W. Lau, Z. Tian, N. Wang and J. Zheng, *Small*, 2023, **19**, 2302055.